A&A, 708, A304 (2026)
https://doi.org/10.1051/0004-6361/202558558

Astronomy & Astrophysics

Resonant and near-resonant dynamics of narrow rings around minor bodies: Symmetric and asymmetric solutions

C. Beaugé[1,2,⋆], E. Gianuzzi[2], M. Cerioni[2], F. A. Zoppetti[1,2], A. M. Leiva[1], and N. Trógolo[1]

[1] Observatorio Astronómico, Universidad Nacional de Córdoba, Laprida 854, (X5000BGR) Córdoba, Argentina
[2] Instituto de Astronomía Teórica y Experimental (IATE), UNC-CONICET, Laprida 854, (X5000BGR) Córdoba, Argentina

Received 12 December 2025 / Accepted 9 March 2026

ABSTRACT

Context. Narrow, dense rings have been detected around several Centaurs and trans-Neptunian objects, and they appear located in the immediate vicinity of spin-orbit resonances (SORs) with the central body. Although resonant motion has not been confirmed, the associated eccentricity excitation may explain several of their dynamical characteristics, including the existence of rings outside of the Roche radius. Adequate models for these commensurabilities are thus necessary.

Aims. While asymmetric librations are known to occur in the circular restricted three-body problem with a Keplerian perturber, it is not clear if the same behavior should be expected in asteroid rings, where the perturber (i.e., nonspherical component) moves in a sub-Keplerian orbit. The aim of this work is thus to extend those classical studies to the case of narrow rings. In particular, our objectives are to study the 1/2 and 1/3 SORs, understand in which cases asymmetric solutions may appear, how they can be adequately modeled, and to analyze their effects on ring dynamics.

Methods. The topology of the SORs was studied using a semi-analytical model for the averaged Hamiltonian extended to the case of a sub-Keplerian perturber. The minor planet was modeled by a spherical body plus a mass anomaly on its surface. Varying both the sign and magnitude of the mass anomaly, we can reproduce a variety of irregular shapes, such as prolate ellipsoids and cratered bodies.

Results. For the 1/2 and 1/3 SORs, we confirm the existence of asymmetric librations for a wide range of rotational frequencies of the mass anomaly. These solutions were found for eccentricities beyond a certain limit, usually on the order of ∼0.01−0.1. For more circular orbits, the phase space does not contain a separatrix, and motion is nonresonant. However, its dynamical behavior shows kinematic librations of the critical angle, and capture is possible under the effect of an exterior nonconservative force. We thus denote these solutions as near-resonance motion. Other SORs, such as the 5/7, are expected to exhibit only symmetric librations.

Key words. methods: analytical – methods: numerical – celestial mechanics – minor planets, asteroids: general – planets and satellites: dynamical evolution and stability

1. Introduction

At the time of writing of this paper, dense and narrow rings have been detected around three outer Solar System minor bodies: Chariklo (Braga-Ribas et al. 2013), Haumea (Ortiz et al. 2017), and Quaoar (Morgado et al. 2023). A more complex structure has been observed around Chiron, although its nature and radial extension is still unclear (Pereira et al. 2025). In all cases, these rings are found very close to spin-orbit resonances (SORs), particularly the $\Omega_0/n = 1/3$ commensurability, where Ω_0 is the spin rate of the central body and n is the orbital frequency of the ring. This proximity to resonance configurations is unlikely to be coincidental, even if the exact formation mechanism is not yet fully understood. Resonance capture is only possible under convergent migration, which in turn requires a significant spin-down of the central body over time (Beaugé et al. 2025). Angular-momentum transfers with the primordial disk (Beaugé et al. 2025) or with an outer satellite (Regály et al. 2025) appear as plausible mechanisms, although both require high masses to counteract the rotational angular momentum of the minor body.

Why rings would prefer the 1/3 SOR over the stronger 1/2 resonance is also uncertain, but possibly linked to the migration mechanism acting on the proto-ring (Sicardy et al. 2019) or resonance overlap leading to orbital instability (G. Madeira, personal communication). To better evaluate this issue, we require a detailed model for the topology (fixed points, stability, resonance width, and so on) of both commensurabilities and an understanding of how these dynamical properties vary as function of system parameters. That is the aim of this paper.

We model the dynamics of the ring by means of the circular restricted three-body problem (CR3BP), in which the minor planet (represented by a spherical body plus a mass anomaly) plays the role of both primaries. In turn, each element of the ring is assumed to be a massless particle, and collisions are neglected at this stage. Since the rotational frequency of the mass anomaly is sub-Keplerian, the resulting dynamics may deviate from the classical CR3BP, rendering any direct extrapolation from classical results unadvisable.

In this dynamical problem, SORs may be considered examples of exterior resonances, in which the perturber is located interior to the orbit of the massless body. The topology of most exterior mean-motion resonances in the classical CR3BP is analogous to that of interior resonances; in other words, it is characterized by symmetric libration points with a single separatrix as described, for example, in Sicardy et al. (2025). However, the structure of the $1/N$ mean-motion resonances (with $N \geq 2$) are different, exhibiting both symmetric and asymmetric librations (Message 1958), and at least two distinct separatrices (Beaugé 1994) delimiting the domain of each libration type. Thus, and at least in the realm of the circular, restricted, three-body problem,

⋆ Corresponding author: cbeauge@unc.edu.ar

both the 1/2 and 1/3 resonances are characterized by asymmetric librations and their dynamics cannot be modeled by a Hamiltonian function with a single resonant term.

In this work we extended these results to the case of SORs with a sub-Keplerian perturber using a semi-analytical Hamiltonian model. We explored the dynamics of the 1/2 and 1/3 SOR for a wide range of rotational frequencies for the minor body and mass ratios. We confirmed the existence of asymmetric libration modes in both commensurabilities, although the eccentricity at which they appear depends on the resonance, spin rate, and perturbing mass. We complemented this theoretical analysis with N-body simulations of resonance capture including an ad hoc exterior force, estimating the necessary eccentricity damping required to reach each resonant domain. In this paper, we discuss the relevance of these results to the known ring systems and speculate on what type of resonant motion could be expected in each case.

2. The Hamiltonian for exterior SORs

We studied the motion of a massless particle (which is denoted by m) orbiting an irregular central body of mass m_0, radius R_0, and rotational frequency Ω_0. We modeled its gravitational potential by the sum of a spherical component plus a mass anomaly of mass, m_1, located at the equator and corotating with m_0. We denote the total mass of the central body as $m_c = m_0 + m_1$ and assume that the orbital plane of the particle coincides with its equator, thus reducing the dynamical problem to a 2D case. Finally, we define the mass factors μ and $\bar{\mu}$ as

$$\mu = \mathcal{G}(m_0 + m_1) = \mathcal{G}m_c \quad ; \quad \bar{\mu} = \frac{m_1}{m_0 + m_1} = \frac{m_1}{m_c}, \tag{1}$$

where $\mathcal{G}$ is the gravitational constant.

In a barycentric (or Jacobi) reference frame, the disturbing function that results from the gravitational perturbation due to the mass anomaly can be written as (e.g., Lee & Peale 2003; Moriwaki & Nakagawa 2004)

$$\mathcal{R} = \frac{\mathcal{G}\,m_0}{|\mathbf{r} + \bar{\mu}\,\mathbf{r}_1|} + \frac{\mathcal{G}\,m_1}{|\mathbf{r} - (1-\bar{\mu})\,\mathbf{r}_1|} - \frac{\mathcal{G}\,m_c}{r}, \tag{2}$$

where $\mathbf{r_1}$ is the m_0-centric position vector of m_1 and $\mathbf{r}$ is the position of m with respect to the center of mass of m_c.

2.1. The Hamiltonian in the extended phase space

We introduce the modified Delaunay canonical variables in the extended phase space, $(L, S, \Lambda, \lambda, -\varpi, \theta_1)$, where λ and ϖ are the mean longitude and pericenter longitude of the particle (respectively), and the angle θ_1 marks the position of the mass anomaly with respect to a fixed (but arbitrary) origin. The momenta associated with the particle's orbit are given by

$$L = \sqrt{\mu a} \quad ; \quad S = L(1 - \sqrt{1-e^2}) \simeq \frac{1}{2}Le^2, \tag{3}$$

with a being the semimajor axis and e the eccentricity, both defined in the barycentric reference frame. The remaining momenta, Λ, is the canonical conjugate of θ_1 and an unknown function. We can then write the Hamiltonian governing the motion of m as

$$F = -\frac{\mu^2}{2L^2} + \Omega_0\Lambda - \mathcal{R}. \tag{4}$$

We assumed that the particle lies in the vicinity of a generic SOR such that

$$\frac{n}{\Omega_0} \simeq \frac{(p+q)}{p}, \tag{5}$$

with p and q being integers. We are interested in exterior resonances where $n/\Omega_0 < 1$, corresponding to integers $q > 0$ and integers $p < 0$. For example, the 1/3 SOR is associated with $(p, q) = (-3, 2)$ while the 1/2 commensurability may be represented by the pair $(p, q) = (-2, 1)$. As with interior resonances, q denotes the order of the SOR.

In the neighborhood of this resonance, it proves useful to introduce a new set of resonant canonical variables $(S, J, \Lambda', \sigma, \sigma_1, Q)$, which are related to the Delaunay variables by

$$\begin{aligned} S &\quad ; \quad q\sigma &&= (p+q)\theta_1 - p\lambda - q\varpi \\ J &= L - S + \Lambda \quad ; \quad q\sigma_1 &&= (p+q)\theta_1 - p\lambda \\ \Lambda' &= (p+q)L + p\Lambda \quad ; \quad qQ &&= \lambda - \theta_1, \end{aligned} \tag{6}$$

which, except for a slight change in notation, are equivalent to those introduced in Beaugé (1994) for exterior mean-motion resonances in the Keplerian CR3BP.

2.2. The averaged Hamiltonian

As it is customary, we averaged the Hamiltonian with respect to the synodic angle Q. The resulting expression F^* is also independent of σ_1 and thus reduces to a single degree of freedom in (S, σ). Both J and Λ' are integrals of motion, but they are written in terms of the undetermined momentum, Λ. We can, however, find a linear combination of both integrals that avoid this problem, and thus we define

$$N = \frac{1}{q}(\Lambda' - pJ) = L + \frac{p}{q}S, \tag{7}$$

which is also an integral of motion and explicitly relates the time variation of L with S.

Introducing the relation $p\Lambda = \Lambda' - (p+q)L$ into expression (4) of the Hamiltonian and disregarding constant terms after averaging, we obtained the following mean resonant Hamiltonian:

$$F^* = -\frac{\mu^2}{2L^2} - \frac{(p+q)}{p}L\,\Omega_0 - \mathcal{R}_{\rm res}, \tag{8}$$

where

$$\mathcal{R}_{\rm res} = \frac{1}{2\pi}\int_0^{2\pi} \mathcal{R}\,dQ \tag{9}$$

is the averaged disturbing function expressed, at least formally, as a function of (S, σ), and is parameterized by N. This integral can be evaluated numerically for each initial condition using the inverse transformation (Beaugé & Michtchenko 2003)

$$M = \sigma + (p+q)Q \quad ; \quad \theta_1 = \sigma_1 + pQ, \tag{10}$$

which relates the synodic angle, Q, with the respective mean anomaly, M, of the particle and the azimuthal angle, θ_1, of the mass anomaly.

Throughout this work, we refrained from using analytical expansions of the disturbing function and calculated the

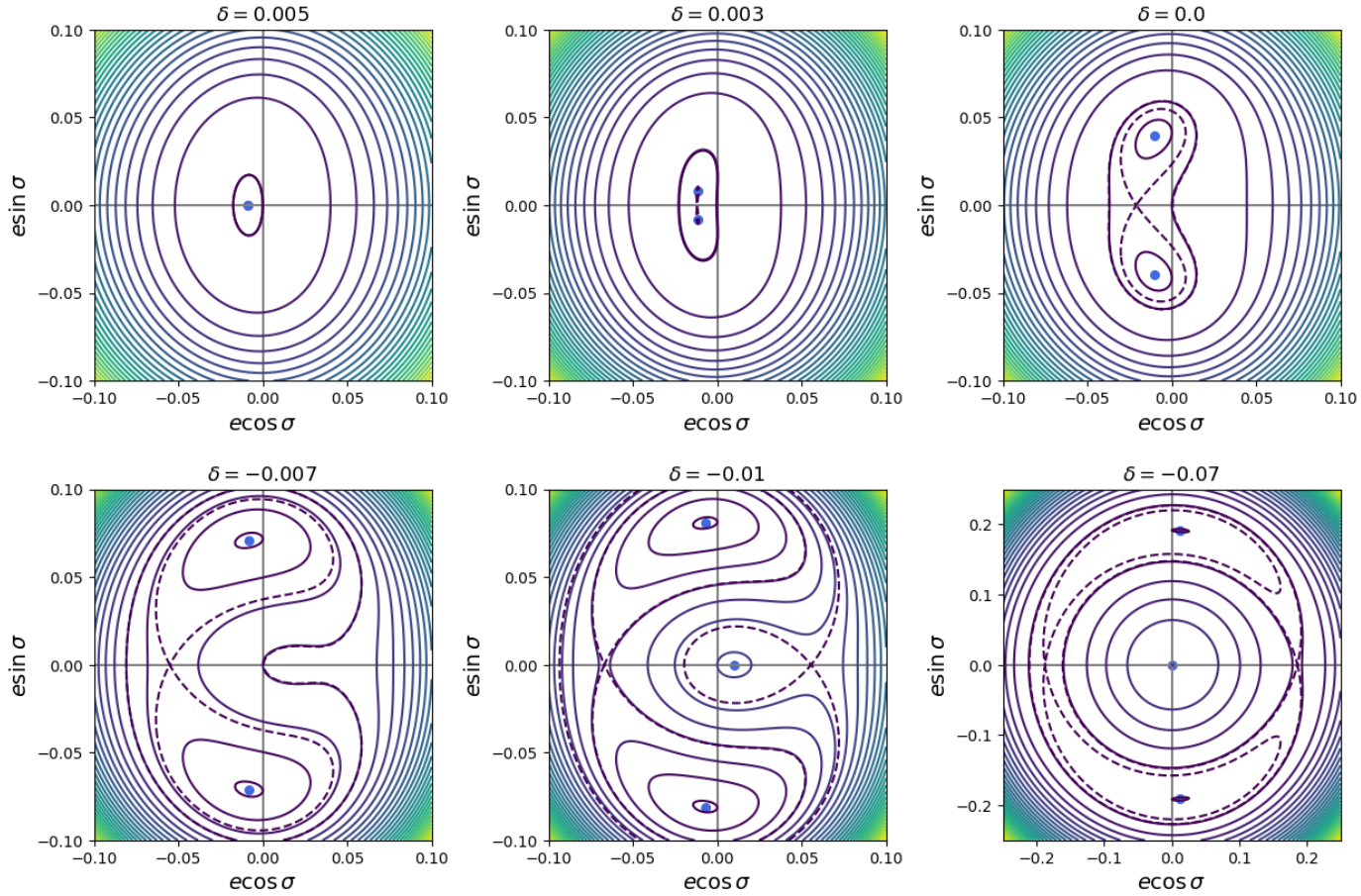

Fig. 1. Structure of the phase plane for the 1/2 SOR for a Quaoar-like central body. All plots were constructed assuming a mass anomaly with $\bar{\mu} = m_1/m_c = 10^{-2}$ and transformed to regular variables $(k, h) = (e\cos\sigma, e\sin\sigma)$. Different values of δ allow us to visualize the transition from symmetric near-resonant motion (top left) to asymmetric libration of increasing eccentricity (bottom right). A second separatrix and an inner circulation region appear at $\delta \lesssim -0.01$. Note the change in the eccentricity limits in the lower-right panel.

averaged Hamiltonian – and the resulting phase space – with this semi-analytical approach. Its greatest advantage is that it avoids any approximation and/or convergence issues related to the expansion of the disturbing function. However, an analytical model for exterior mean-motion resonances, based on the Andoyer Hamiltonian (Andoyer 1903), can be found in Beaugé (1994).

3. The phase space for the 1/2 SOR

We began by applying our semi-analytical model to the 1/2 SOR and probing the phase plane (S, σ), as a function of N. Instead of using N, we can also characterize each plane by

$$\delta = \frac{N^2}{\mu a_{\rm res}} - 1, \tag{11}$$

where $a_{\rm ares}$ is the semimajor axis associated with exact resonance, i.e., $\sqrt{\mu/a_{\rm res}^3} = \Omega_0(p+q)/p$. This parameter is equal to zero at the nominal location of the SOR, and it takes positive (negative) values for semimajor axes larger (smaller) than $a_{\rm res}$.The value of δ for which the libration region first appears is thus indicative of the width of the SOR for near-circular orbits.

Perhaps a better way to visualize the proximity to exact resonance is to introduce the resonance offset (Ramos et al. 2017), which, in the case of SORs, acquires the form

$$\Delta_{(p+q)/p} = \frac{n}{\Omega_0} - \frac{(p+q)}{p}. \tag{12}$$

As with δ, this new metric is also zero at the nominal value of exact resonance, but it measures the distance of each solution in the domain of mean-motion ratios, instead of the semimajor-axis, which can be less intuitive.

Figure 1 shows the structure of the phase plane drawn for six different values of δ assuming a Quaoar-type system. The total mass and radius of the central body were taken as equal to $m_c = 1.4 \times 10^{21}$ kg and $R_0 = 555$ km, respectively (Fraser et al. 2013). Assigning a value to the spin rate is trickier, since observations are consistent with both $2\pi/\Omega_0 \simeq 8.84$ h and $2\pi/\Omega_1 \simeq 17.67$ h (e.g., Ortiz et al. 2003; Kiss et al. 2024), depending on a single- or double-peak solution of the light curve. Since the 1/3 SOR is consistent with the larger period, we generally assumed this value, but both were studied.

For $\delta = 0.005$ (top-left panel), the system has not yet entered the resonant domain, and no separatrix is observed. The resulting topology is equivalent to a non-resonant torus, although the single, stable fixed point appears displaced from the origin toward a value of $\sigma = \pi$. By analogy with interior resonances (e.g., Morbidelli & Moons 1993), we call this family of near-resonant solutions the apocentric branch.

Under the effect of a nonconservative force, this center morphs into an attractor leading to what are generally known as kinematical librations (e.g., Henrard & Lemaitre 1983). Different from dynamical libration, in this case there is no separatrix crossing and the phase space has the same topological structure as the non-resonant case. A body exhibiting a small-amplitude oscillation (or kinetical libration) around such a fixed point is sometimes denoted as near-resonant, a term we will adopt here. As we will show later on, even in this near-resonant domain, the system is able to capture particles undergoing migration, displaying orbital behavior very similar to resonant motion.

As the system approaches the true resonant domain ($\delta \simeq 0$), the stable fixed point at $\sigma = \pi$ bifurcates into two asymmetric solutions with critical angles that seem to approach $\sigma \simeq \pm\pi/2$ for higher eccentricities and increasingly negative values of δ. This change in topology is accompanied by the appearance of a first separatrix, stemming from the hyperbolic unstable point located at $\sigma = \pi$, and encompassing both asymmetric libration points. It is important to stress that this bifurcation of the original near-resonant apocentric branch into asymmetric solutions does not occur in other first-order exterior SORs such as the 2/3 or 4/5, but is only observed in the 1/2 commensurability.

At smaller values of δ a second separatrix appears, stemming from a new hyperbolic fixed point located at $\sigma = 0$. The resulting structure is reminiscent of the classical topology associated with interior resonances, including the appearance of an inner circulation region close to the origin. The new (symmetric) libration region encompasses the asymmetric structure, allowing for large-amplitude oscillations around $\sigma = \pi$ even if the fixed point located at this value is unstable. These results are analogous to those described in Beaugé (1994), even though here we considered a perturbing mass of m_1 in a sub-Keplerian circular orbit.

We stress two important characteristics of the dynamics of the 1/2 SOR. First, contrary to interior resonances and other exterior first-order commensurabilities, all dynamical librations are asymmetric, and the only solutions that display oscillations around $\sigma = \pi$ correspond to near-resonant motion. Second, both asymmetric islands are independent, and resonance capture can occur in either without displaying oscillations around the other.

3.1. Symmetric and asymmetric librations

We now focus on the locus of stable fixed points, σ, as a function of the proximity indicator δ and, thus, the eccentricity, as well as the appearance of both separatrices. Results are shown in Fig. 2 for the same system parameters employed in Fig. 1. The top panel shows the loci of stable solutions (continuous curves) and unstable fixed points (dashed lines) as a function of δ. Resonance-offset, $\Delta_{1/2}$, and associated values are depicted in the top axis. The vertical beige lines highlight the values of δ adopted for each of the phase planes shown in Fig. 1.

The bottom panel of Fig. 2 shows the resonant angle of the stable fixed points associated with the global minimum of the Hamiltonian as function of the eccentricity. We identify two possible critical values of the eccentricity:

- $e_{\rm dyn}$, or minimum eccentricity for dynamical libration, specifies the upper limit of the near-resonant domain. True dynamical librations and resonant separatrices are found only for eccentricities beyond this value, while all librations observed at more circular orbits are kinematical.
- $e_{\rm asym}$, or minimum eccentricity for asymmetrical libration, defines the minimum eccentricity at which asymmetric librations appear.

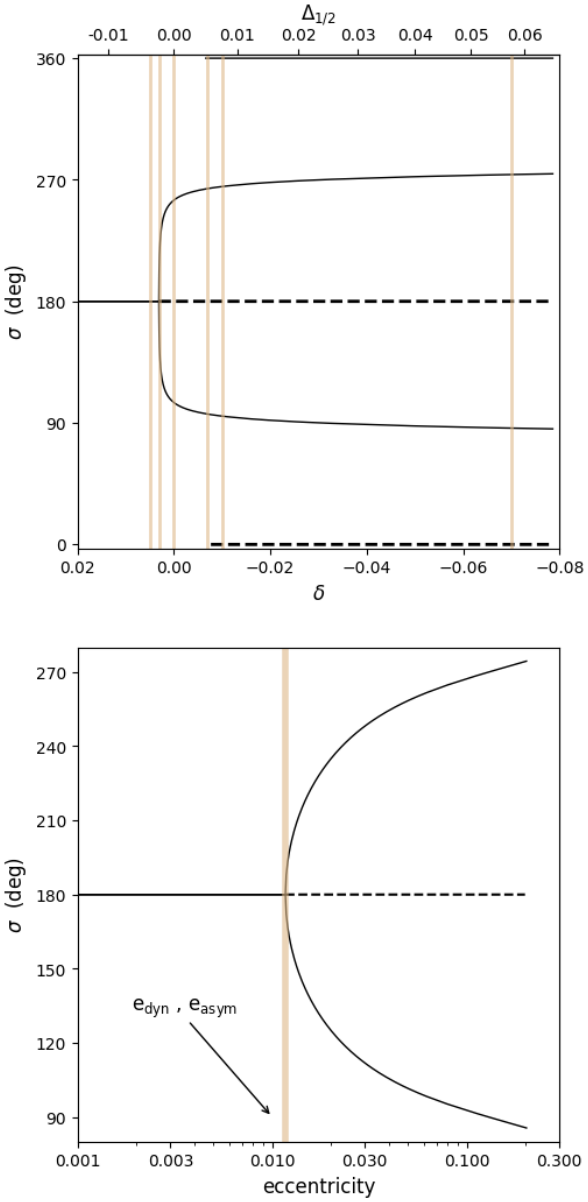

Fig. 2. Top: resonant angle, σ, corresponding to stable (continuous lines) and unstable (dashed lines) fixed points for the 1/2 SOR as function of δ. Since both unstable and stable solutions exist at $\sigma = 0$ for $\delta \lesssim -0.07$, the first was plotted at $\sigma = 0$, while the second was plotted at $\sigma = 360°$. Vertical beige lines identify the mapped values of δ adopted for the phase planes in Fig. 1. System parameters were also preserved from that figure. Bottom: values of σ as a function of the eccentricity for the global minimum of F at each value of N (or δ). The bifurcation from symmetric to asymmetric librations occurs at $e = e_{\rm asym}$.

For the 1/2 SOR both limits are equal, and there is no interval in which symmetric dynamical librations exist. However, in other SORs, including the 1/3 commensurability, these values will be different.

These results show that the topology of the 1/2 SOR may be divided into two distinct regions. Particles with eccentricities below the critical value $e_{\rm dyn} = e_{\rm asym}$ are located in the near-resonant domain, even if the resonant angle displays kinematic librations around $\sigma = \pi$. On the other hand, all resonant motion is associated with asymmetric librations, mean eccentricities above the critical value, and librations of σ around one of

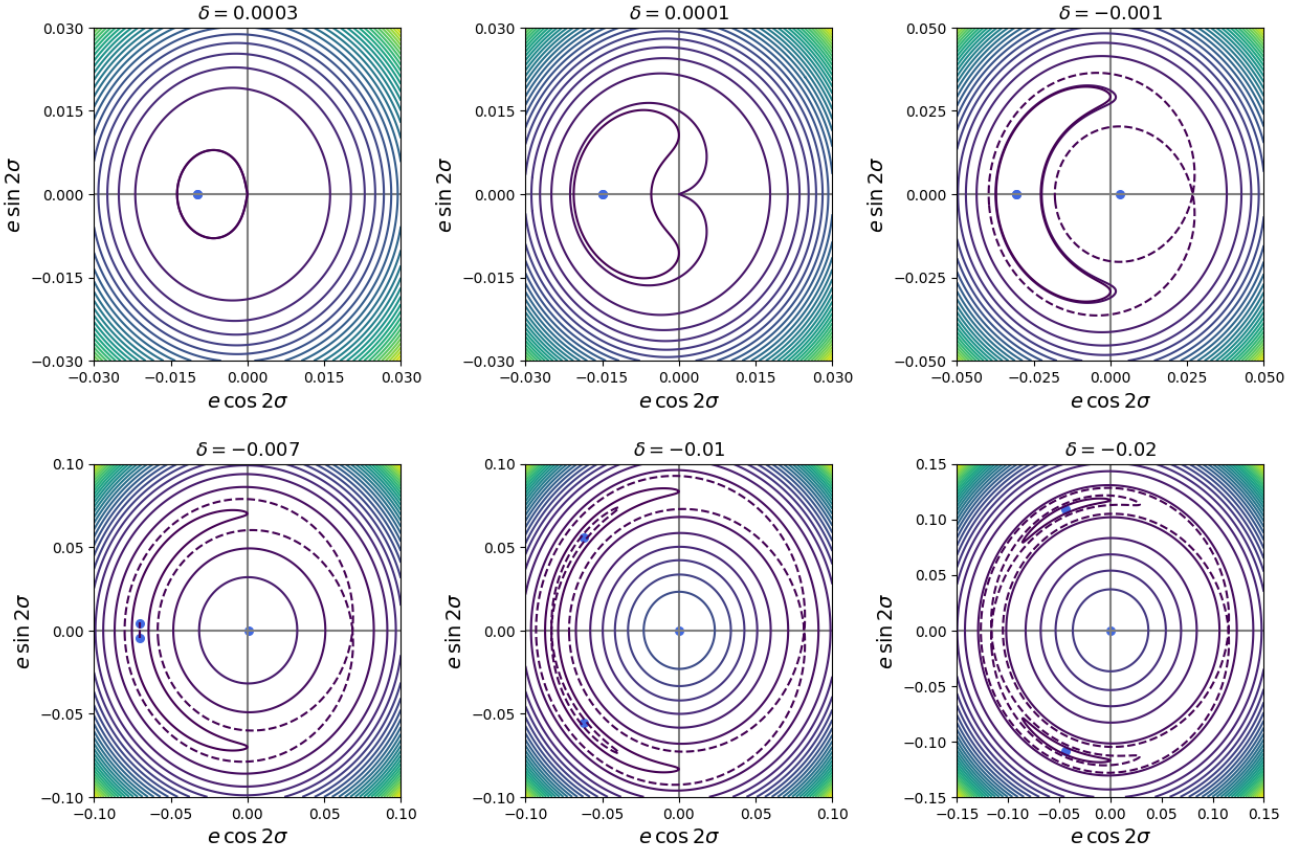

Fig. 3. Structure of the phase plane $(k, h) = (e\cos 2\sigma, e\sin 2\sigma)$ for the 1/3 SOR for a Quaoar-like central body. All plots were constructed assuming a mass anomaly with $\bar{\mu} = m_1/m_c = 10^{-2}$. Different values of δ allow us to visualize the transition from symmetric near-resonant motion (top left) to asymmetric libration of increasing eccentricity. The separatrices are highlighted with dashed lines. Contrary to the 1/2 SOR, the low-eccentricity dynamical librations are symmetric, while the asymmetric domain only appears for $e \gtrsim 0.07$. Note the change in the eccentricity limits in the different frames.

two equilibrium points. These values rapidly depart from $\sigma = \pi$ and acquire values close to $\sigma \sim \pi$ and $\sigma \sim 3\pi/2$.

4. The phase space for the 1/3 SOR

We now turn to the 1/3 SOR, in whose vicinity most of the minor body rings are found. Figure 3 shows six different phase planes of F^* level curves, each drawn for a different value of δ. As before, we choose to present the results in non-canonical regular variables, now defined as $(k, h) = (e\cos q\sigma, e\sin q\sigma)$, where $q = 2$ is the order of the resonance. Contrary to common practice, we have chose to plot the resonant structure in terms of $q\sigma$ instead of σ in order to boost simplicity and gain clarity. In the circular problem, all resonant terms associated with a q-order commensurability appear as $q\sigma$, making this the representative angular variable instead of σ. This choice also helps to highlight the size of the libration domains and avoid the appearance of multiple mirror islands.

As with the 1/2 SOR, the top-left panel shows the phase plane for a value of δ prior to the emergence of the first separatrix (dashed curve) and the resonant domain. Similarly to the 1/2, the topology is akin to non-resonant motion with a single stable center displaced from the origin. Note that the equilibrium value lies at $q\sigma = 2\sigma = \pi$, thus corresponding to the classical values $\sigma = \pi/2$ and $\sigma = 3\pi/2$.

As δ decreases, the resonant domain and the first separatrix appear, somewhere between the top-center and top-right panels. Contrary to the 1/2 SOR, the first dynamical librations are symmetric and centered at $2\sigma = \pi$. This behavior is typical of other second-order exterior resonances (such as the 5/7), as well as their interior counterparts. Thus, at this point there is no indication of any novel feature in the 1/3 SOR that deserves additional attention.

Things change, however, as δ decreases even further and immerses even deeper into the resonance region. At $\delta \simeq -0.007$ (bottom-left panel), the symmetric solution at $2\sigma = \pi$ becomes unstable, giving birth to a second separatrix and a pair of asymmetric stable libration points. As δ continues to decrease, the resonant angles continue to deviate from the apocentric branch, reaching $2\sigma \simeq \pi/2$ for high eccentricities. As with the 1/2 SOR, each asymmetric libration island is independent, and capture into one is restricted to its domain and will not leak over to its neighbor. Only under very specific initial conditions would a massless particle display a large-amplitude oscillation around both asymmetric libration islands, apparently centered around the hyperbolic symmetric solution. Such dynamical behavior is akin to a horseshoe-type motion around the L_3 Lagrange point, but occurring in the 1/3 commensurability.

4.1. Symmetric and asymmetric librations

As in the Keplerian CR3BP, both the 1/2 and 1/3 SOR are characterized by asymmetric librations and multiple separatrices. There are, however, significant differences between the two

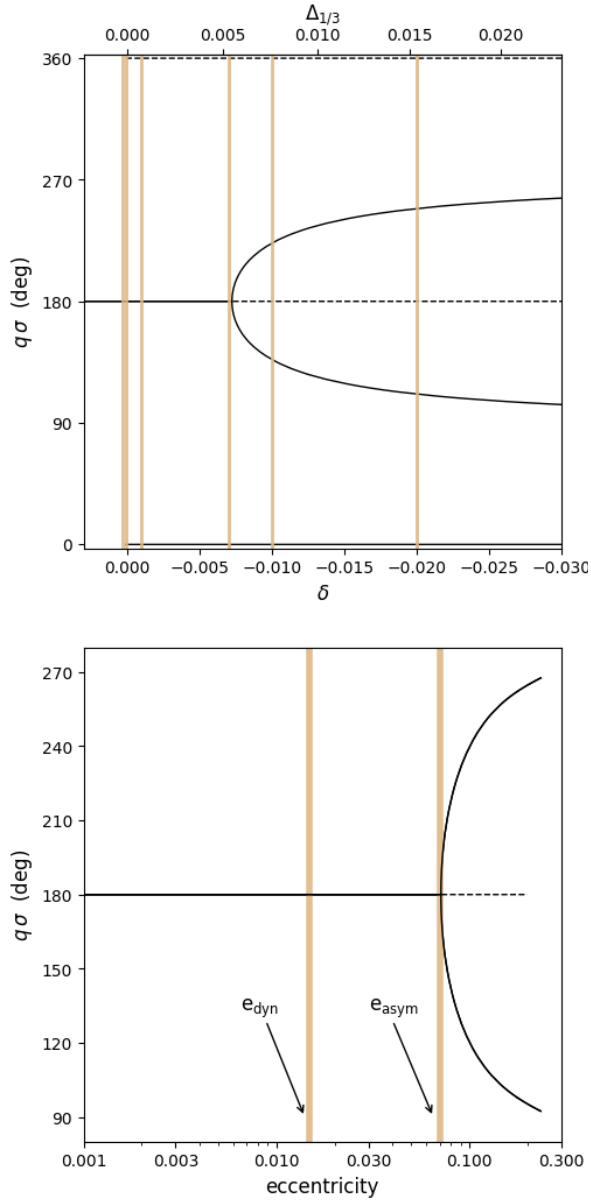

Fig. 4. Top: resonant angle, σ, corresponding to stable (continuous lines) and unstable (dashed lines) fixed points for the 1/3 SOR as function of δ. As observed in the 1/2 SOR, both unstable and stable solutions are detected at $q\sigma = 0$ for $\delta \lesssim 0$. We thus plotted the stable branch at $q\sigma = 0$, while the unstable solutions are shown at $q\sigma = 360°$. Vertical beige lines identify the mapped values of δ adopted for the phase planes in Fig. 3. System parameters were also preserved from that figure. Bottom: values of σ as function of the eccentricity for the global minimum of F at each value of N (or δ). The conversion from kinematical to dynamical librations occurs at $e = e_{\rm dyn}$, while the bifurcation from symmetric to asymmetric librations occurs at $e = e_{\rm asym}$.

resonances. While in the 1/2 case all small-amplitude librations are asymmetric, the 1/3 SOR exhibits symmetric dynamical librations for eccentricities below a certain limit, $e_{\rm asym}$, which is higher than the value $e_{\rm dyn}$, at which kinematical librations cease to exist.

Figure 4 presents a bifurcation diagram for the 1/3 SOR, once again assuming Quaoar-like system parameters. The top panel shows the different stable (continuous lines) and unstable (dashed lines) solutions as function of δ. The vertical beige lines highlight the values of δ adopted for each of the phase planes shown in Fig. 3. The resonance offset $\Delta_{1/3}$, as defined by expression (12), is given on the top axis. The change in stability of the $q\sigma = \pi$ symmetric solution, and its bifurcation into asymmetric stable solutions is not so abrupt as in the 1/2 resonance, and the limit $2\sigma \to \pi/2$ requires much smaller values of the offset and, as noted below, much higher eccentricities.

The bottom panel focuses on the dependence of the minimum-Hamiltonian stable solutions as a function of the eccentricity. These are the libration points that are expected to house captured particles under the effects of an exterior non-conservative force. This plot clearly shows the three distinct libration domains as a function of e. For eccentricities $e < e_{\rm dyn}$, all librations are kinematical and not truly resonant, even if the capture process could still take place and the resonant angle exhibit small-amplitude oscillations around $2\sigma = \pi$. Dynamical symmetric librations around the same value of σ are expected in the $e \in [e_{\rm dyn}, e_{\rm asym})$ interval, displaying a resonant structure analogous to interior resonances. Finally, asymmetric librations appear for $e \geq e_{\rm asym}$, and a second separatrix emerges inside the symmetric domain. Higher eccentricities are accompanied by increasingly asymmetric librations, while no stable solutions remain in the symmetric region.

4.2. Dependence on mass and rotation

So far we have analyzed the structure of the 1/2 and 1/3 SOR assuming system parameters inspired in present-day Quaoar. We now focus on the 1/3, analyzing how the resonant domains, as characterized by the dynamical and asymmetric eccentricities, vary as a function of both the magnitude of the mass anomaly $\bar{\mu}$ and the rotational frequency Ω_0. This last parameter allowed us to measure how the structures in the sub-Keplerian problem deviate from the classical CR3BP.

In turn, $\bar{\mu}$ not only made it possible to assess the magnitude of the gravitational perturbation, it allowed us to smoothly transition between different models for irregular central bodies. Thus, while positive values of $\bar{\mu} < 1/2$ correspond to a spherical body with a mass anomaly, negative values could be prompted to simulate the potential of a spherical body with a crater. Alternatively, taking $\bar{\mu} = 1/2$ generates a gravitational potential analogous to that of a C_{22} term in an expansion in spherical harmonics, and thus may be considered a good model for a prolate ellipsoidal equilibrium figure. Thus, the Hamiltonian F^* given by Eq. (8) may be employed to describe different types of irregular central bodies.

It is also worthwhile to note that neither the total mass, m_c, nor the radius, R_0, are, in themselves, relevant parameters of these solutions. Both may be considered as scaling factors of the Hamiltonian, and their individual values do not enter in the calculations of the position or stability of the fixed points of F^*. Consequently, the results discussed in this section should be applicable to all the ring systems detected around minor bodies.

Figure 5 shows the variation of both critical eccentricities, in the case of the 1/3 SOR, as function of the rotational frequency Ω_0 of the central body. The beige vertical lines highlight the rotational frequencies of all minor bodies currently known (or believed) to host narrow rings. The two lines drawn for Quaoar correspond to both proposed spin rates.

Each colored curve was calculated adopting a different mass anomaly, $\bar{\mu} = m_1/m_c$, whose magnitude is overlaid to the $e_{\rm dyn}$ curves. This proved unnecessary for $e_{\rm asym}$ since all values are practically independent of the perturbing mass. This seems to indicate that the limit between symmetric and asymmetric librations is extremely robust, and its value should be a

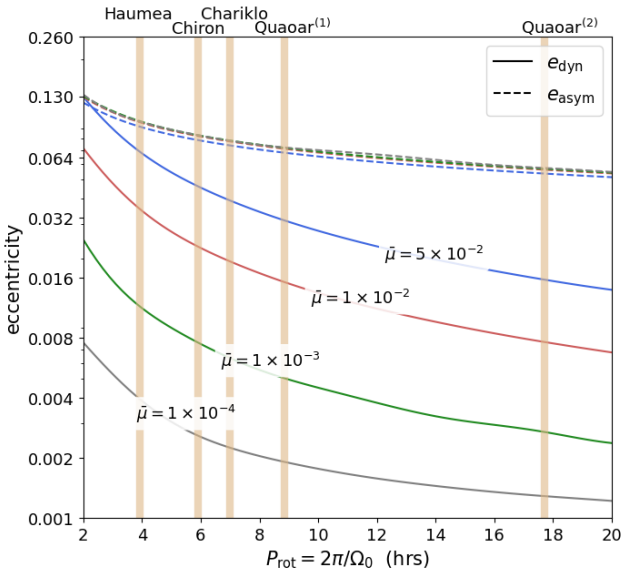

Fig. 5. Critical eccentricities for the 1/3 SOR, associated with changes in the resonant domain, as function of the rotational period of the central body. Different colored curves correspond to different values for the mass anomaly $\bar{\mu} = m_1/m_c$. The rotational periods for the minor bodies with rings and/or disks are highlighted with vertical beige lines. The values of e_{dyn} mark the first appearance of dynamical librations, while e_{asym} signal the bifurcation of symmetric librations (at $q\sigma = \pi$) and the appearance of asymmetric solutions.

well-established quantity for all real systems regardless of the ambiguities in estimating the size and type of mass anomaly.

Both critical eccentricities, however, decrease as a function of the rotational period, although this trend is more pronounced for e_{dyn}. The asymmetric limit is surprisingly robust, and we predicted values of $e_{asym} \sim 0.07-0.1$ for all minor bodies. If the eccentricities of the rings are confirmed to lie below these values, then asymmetric librations can be ruled out in these systems.

The critical eccentricity $e_{dyn,}$ is much more dependent on system parameters, reaching very low values for $\bar{\mu} \sim 10^{-4}$ or lower. However, relatively high values are also possible for rotational periods on the order of a few hours, especially for mass anomalies of $\bar{\mu} \sim 10^{-2}$. Thus, depending on the ellipticity of ring particles, it is possible that any resonant motion in these systems is actually related to kinematical librations and no separatrix crossing occurred. However, as we show in the next section, this would imply a migration mechanism with a very strong eccentricity damping.

Note that as $\bar{\mu}$ increases, the minimum eccentricity required for dynamical libration approaches e_{asym}. In the limiting case where $\bar{\mu} = 0.5$, corresponding to the maximum allowed value, the continuous and dashed curves nearly overlap. This behavior implies that symmetric librations become increasingly rare for larger $\bar{\mu}$, and they are progressively replaced by their asymmetric counterparts with $2\sigma \to \pi/2$.

5. Resonance width and the apocentric branch

In Fig. 6, we study the resonant structures of the 1/2 (top) and 1/3 (bottom) SORs by means of Δe dynamical maps in two $(\Omega_0/n, e)$ representative planes. The left panels correspond to initial conditions of the resonant angle $q\sigma = \pi$, while $q\sigma = \pi/2$ was adopted for the right-hand graphs. The first is expected to map the symmetric fixed points and the structure of the phase space in their vicinity, while the second focuses on the asymmetric librations. Even though the resonant angle of asymmetric fixed points is not equal to $q\sigma = \pi/2$, they are sufficiently close to reproduce the main properties of the system at these values.

The color-mesh in each plot shows the result of the N-body integration (i.e., Newtonian equations of motion in the barycentric reference frame) of a grid of 200×200 initial conditions integrated for a total timescale of 200 years, corresponding to more than 10^4 orbital periods. The color-code shows the maximum incursion in eccentricity during the integration time:

$$\Delta e = \max(e(t)) - \min(e(t)). \tag{13}$$

This dynamical indicator introduced by Dvorak et al. (2004) is a very simple but powerful method to map complex dynamical systems. Fixed points of the averaged Hamiltonian are associated with very small changes in the eccentricity and appear with dark colors. Conversely, initial conditions leading to large incursions in eccentricities, such as close to the separatrix, appear colored with light tones. While it is not designed to identify chaotic or unstable regions, Δe allows us to identify resonant structures including periodic orbits and libration widths.

All maps show the classical V-shape structure defined by both branches of the separatrix. Initial conditions inside are typically resonant with different amplitudes of oscillation, while those outside are non-resonant. Nevertheless, the maps for $q\sigma = \pi$ and $q\sigma = \pi/2$ show significant differences; their properties may be understood with the semi-analytical model. Zero-amplitude solutions (i.e., fixed points) on the averaged Hamiltonian correspond to periodic orbits in the dynamical maps.

The red curves show the loci of zero-amplitude solutions of F^*, with symmetric ones on the left and asymmetric ones on the right. A very good agreement is observed with the dark regions in the dynamical maps, both in the 1/2 and the 1/3 SORs. By analogy with interior resonances (e.g., Morbidelli & Moons 1993), we refer to the symmetric solutions as the apocentric branch. It contains both kinematical and dynamical librations. As with interior resonances, the apocentric branch in the first-order commensurabilities extends well beyond the nominal location, $\Omega_0/n = p/(p+q)$, and its presence helps guide the particles into the resonant domain when under the effects of a convergent migration. In second-order resonances, the kinematical librations are less extended, and the 1/3 SOR is no exception. However, differently from interior resonances, in the 1/2 SOR the apocentric branch is broken by the first separatrix, and only kinematical librations appear in the $q\sigma = \pi$ representative plane, while the dynamical librations appear in the right-hand plot. This explains why the dynamical map in the vicinity of the nominal resonance point $\Omega_0/n = 2/1$ is only associated with small values of Δe in the right panel, while it corresponds to larger eccentricity amplitudes for initial conditions with $q\sigma = \pi$.

The black lines in both of the top dynamical maps show the branches of the first (symmetric) and second (asymmetric) separatrices. The correlation with the numerical simulations is again very good, at least generally speaking. Note, however, that for asymmetric librations the width of the separatrix is not always located close to $q\sigma = \pi/2$, and thus it does not always coincide with the initial conditions chosen for the map.

The two lower frames correspond to the 1/3 SOR. The resonant structure is different, and both the dynamical map and the semi-analytical model agree. Although the apocentric branch is again separated between kinematical and dynamical librations, both are symmetric and are observed in the left panel. The second separatrix is now linked to the asymmetric solutions and

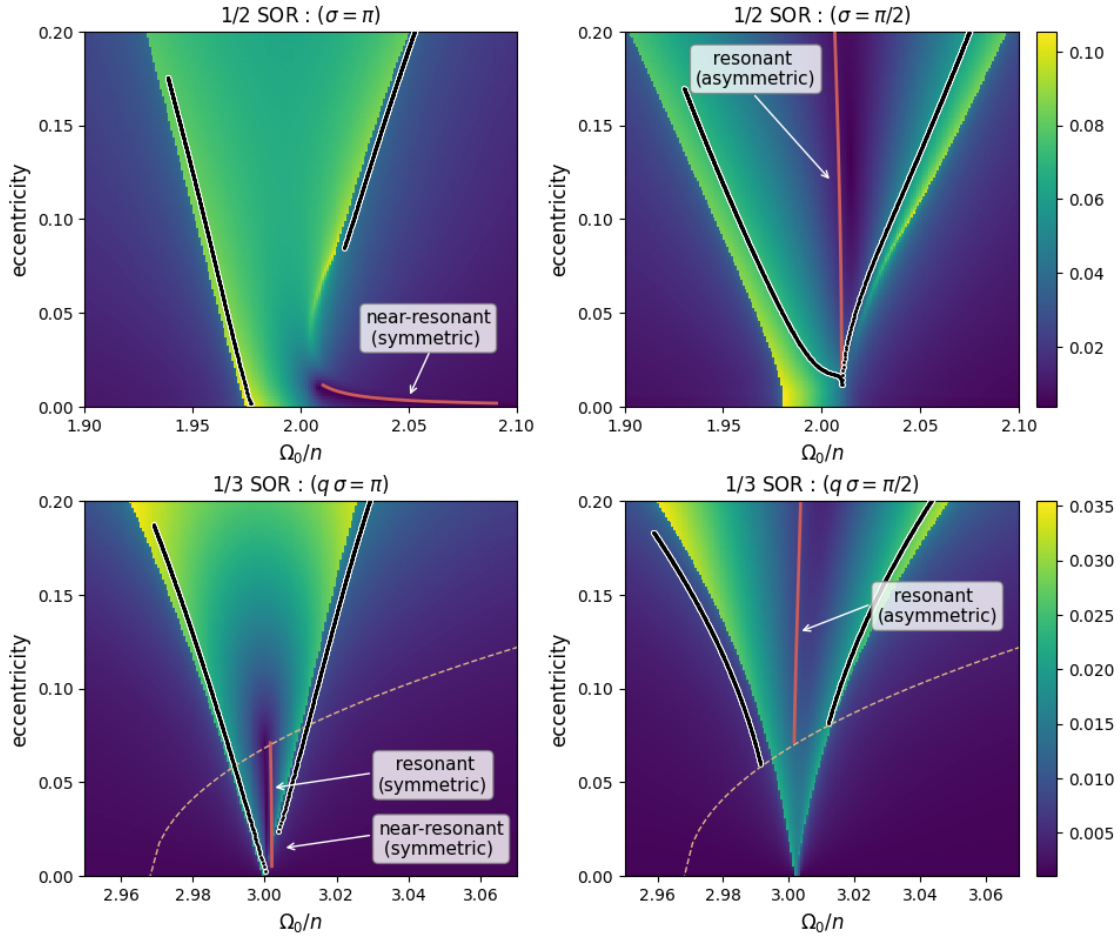

Fig. 6. Δe dynamical maps, each drawn for a grid of initial conditions in the $(\Omega_0/n, e)$ plane, with angles such that $q\sigma = \pi$ (left panels) and $q\sigma = \pi/2$ (right). As before, we assume a mass anomaly characterized by $\bar{\mu} = m_1/m_c = 10^{-2}$. Top panels: results for the 1/2 SOR. Bottom: results for the 1/3 SOR. The color-code indicates the maximum value of Δe attained in the integration time ($T = 200$ yrs). Black curves are the semi-analytical estimations of both sets of separatrices; those associated with symmetrical solutions are plotted in the left panels; while those encompassing asymmetrical solutions are shown in the right. Red lines correspond to the locus of zero-amplitude libration points, again with the symmetric ones on the left and asymmetric ones on the right. The different resonant domains (near-resonant, symmetric resonant, and asymmetric resonant) are identified with the aid of inlaid labels.

thus appears in the right panel for values of $\delta < 0$. This value also signals the transition of the family of stable solutions (red curve) from the left- to the right-hand plot. Thus, the set of initial conditions with $\delta = 0$, here drawn with dashed beige curves, mark the boundary between both resonant domains.

6. Resonance capture and evolutionary routes

Having established the structure of the 1/3 SOR, we turned our attention to the capture process under the effects of an exterior nonconservative force. In particular, we wanted to understand which of the different resonant domains may host captured bodies and what the necessary conditions for the migration are in each case. However, it must be noted that the simulations present here are purely illustrative and are not expected to realistically model the dynamical evolution of proto-ring particles.

Since resonance capture requires convergent migration, we simulated the combined particle and minor body rotational evolution by an ad hoc exterior force acting on the massless particle (see Beaugé et al. 2006) and characterized by a semimajor axis decay and an eccentricity damping timescales τ_a and τ_e, respectively. Provided the nonconservative evolution is adiabatic with respect to the resonance dynamics, the relevant parameter for the outcome is given by the ratio

$$\mathcal{K} = \frac{\tau_a}{\tau_e} \tag{14}$$

(see, e.g., Lee & Peale 2002; Beaugé et al. 2006), while the individual values of the timescales only serve to set the timescale of the capture process.

Figure 7 shows the results of three N-body simulations, where the orbits are propagated according to the Newtonian equations of motion ($N = 3$) and the ad hoc exterior nonconservative force as described in Beaugé et al. (2006). Each simulation adopted different values for $\mathcal{K}$. In all cases, the orbital decay characteristic time was maintained fixed at $\tau_a \sim 10^5$ yr, while the eccentricity damping timescale was varied. For the central mass, we again adopted a Quaoar-like body, with a mass anomaly equal to $\bar{\mu} \equiv m_1/m_c = 5 \times 10^{-2}$. Initial conditions for the particles were chosen such that $\Omega_0/n = 3.25$, eccentricity $e = 0.01$ and all angles equal to zero.

Results show that, while resonance capture is possible in the three cases we analyzed, the resonant domain in which the captured body is ultimately housed (near-resonant, symmetric, or

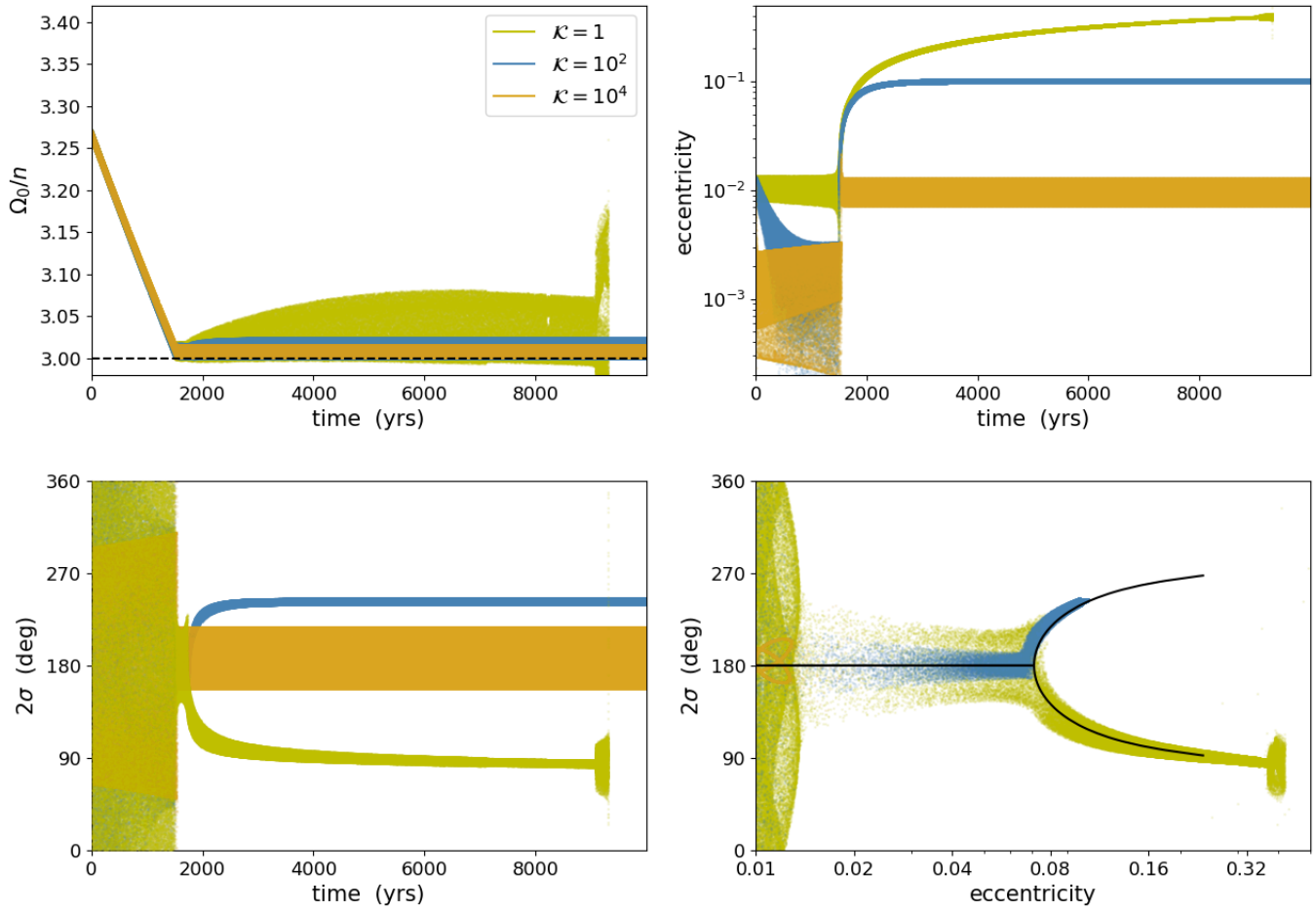

Fig. 7. Three N-body simulations of massless particles captured in the 1/3 SOR under the effects of an ad hoc exterior dissipative force. The central body is represented by a spherical component plus a mass anomaly with $\bar{\mu} = 5 \times 10^{-2}$. Each simulation is characterized by a different value of $\mathcal{K} = \tau_a/\tau_e$, as shown in the legend in the top-left panel. Although all simulations lead to resonance capture in the 1/3 SOR, the final outcome is a strong function of $\mathcal{K}$. For very weak eccentricity damping, the resonant orbit is unstable and the particle is ejected after its eccentricity surpasses $e \sim 0.3$. Stable orbits are found for larger values of $\mathcal{K}$, although in different libration modes. A very strong eccentricity damping is required for a symmetric libration around $\sigma = \pi$. Weaker damping leads to asymmetric librations. Note that both asymmetric lobes are populated, though only temporarily for one of them.

asymmetric) is a strong function of $\mathcal{K}$. In particular, the final eccentricity is defined by the equilibrium value at which the damping force is equal to the eccentricity excitation induced by the SOR.

For very weak eccentricity damping (e.g., $\mathcal{K} = 1$, green curves), the exterior force is unable to counteract the eccentricity excitation induced by the resonance. The resonant orbit thus travels along the apocentric and asymmetric branches until it suffers a close encounter and is ejected. This occurs approximately when the eccentricity surpasses $e \sim 0.3$. Stable orbits are found for larger values of $\mathcal{K}$, although in different libration modes. A very strong eccentricity damping is required for a symmetric near-resonance libration around $2\sigma = \pi$ (orange curve). Weaker damping leads to an asymmetric libration, in this case with $2\sigma \simeq 3\pi/2$ (blue curve). Note that capture in any asymmetric lobe is possible, and which one is actually chosen by the particle appears to be the result of a stochastic process.

In problems of type-I disk-induced planetary migration, the value of $\mathcal{K}$ is primarily defined by the disk scale-factor H_R, and it usually takes values on the order of $\mathcal{K} \sim 10^2$ (e.g., Baruteau et al. 2014). In the present case, however, each characteristic timescale τ_a and τ_e is defined by a different physical process. Eccentricity damping is dominated by the collisional drag. Adopting the simple prescription (Sicardy et al. 2019), we may express the acceleration suffered by the particle due to collisions as

$$\ddot{\mathbf{r}}_{\rm col} = -\eta n \dot{r} \hat{\mathbf{r}}, \tag{15}$$

where $\mathbf{r}$ is the barycentric position vector of the particle being studied, n its mean motion, and η a dimensionless coefficient related to the particle size and density profile at the location. More details may be found in Sicardy et al. (2019) and Salo et al. (2021). Introducing Expression (15) into Gauss's variational equation for the eccentricity (e.g., Beutler 2005), we obtain, after averaging over an orbital period,

$$\frac{de}{dt} = -\frac{1}{2}\eta n e \quad \rightarrow \quad \tau_e = \frac{2}{\eta n}. \tag{16}$$

Note that we took τ_e as positive even though the effect of the exterior force is a decrease in the eccentricity, and its value is inversely proportional to the drag coefficient, η.

The orbital decay timescale (relative to the resonance location), τ_a, on the other hand, is the net result of two competing

effects. On one hand, as shown in Beaugé et al. (2025), the interaction between the collision drag and the semi-forced eccentricity gradient $e_{\rm SF}(a)$ generates an outward migration of the particle and thus a divergent migration with respect to the resonance location. On the other hand, the spin-down of the central body generates the opposite effect. Resonance capture can only occur under a net convergent migration, but its characteristic timescale will be a function of both effects. Since we presently lack an analytical expression for both $e_{\rm SF}(a)$ as well as credible values for the rotational spin-down rate, we cannot estimate what values of $\mathcal{K}$ are expected for the capture process of asteroid rings and, thus, what type of resonant motion we would expect for these systems.

7. Conclusions

In this work, we analyzed the structure of the 1/2 and 1/3 SORs in the circular, restricted three-body problem with a sub-Keplerian perturber. We found that both commensurabilities show the existence of stable symmetric $q\sigma = \pi$, asymmetric libration points, and two independent separatrices. Asymmetric solutions were found for eccentricities $e \geq e_{\rm asym}$, whose value is on the order of 0.1 for the 1/3 SOR, but significantly lower for the 1/2 resonance. The precise limit between both domains, however, depends on the perturbing mass, $\bar{\mu}$, and the spin rate, Ω_0, of the central body.

Even though both commensurabilities exhibit distinct libration modes, their structure at low eccentricities is different. Dynamical librations first appear as asymmetric in the 1/2 SOR, yet symmetric in the 1/3. For even lower eccentricities, all librations are kinematical and cannot be considered truly resonant. Notwithstanding this point, resonance capture can occur in this near-resonant domain, provided the eccentricity-damping mechanism is sufficiently strong.

N-body simulations with ad hoc nonconservative forces show that resonance capture in the 1/3 SOR is possible under a wide range of parameters, provided two conditions are met: (i) orbital variation with respect to the location of the SOR is convergent; and (ii) the mass anomaly, $\bar{\mu}$, is sufficiently large that resonant perturbations are able to counteract the migration. Capture probability is increased if the process is adiabatic, requiring slow orbital variations as compared to the librational periods.

The outcome of the resonance capture is found to depend on the eccentricity damping strength, as characterized by the adimensional parameter $\mathcal{K} = \tau_a/\tau_e$. Stable solutions are found only for sufficiently high eccentricity damping, such that $\mathcal{K} \gtrsim 1{-}10$. Similar limits were found in the 1/2 SOR.

The magnitude of eccentricity damping also determines the type of resonant solution acquired by the particle, be it symmetrical, asymmetrical, or kinematical. Current estimates of the eccentricity of asteroid rings range between 10^{-3} and 10^{-2} (e.g., Morgado et al. 2021; Pereira et al. 2023), which are consistent with kinematical librations and near-resonant dynamics. However, a quasi-circular ring does not preclude the possibility of eccentric individual particles, provided the pericenters are not aligned. The nature of the resonant dynamics in asteroid rings is thus not only diverse, but at present also unconstrained.

Acknowledgements. The simulations discussed in this work were carried out with the computing facilities hosted at IATE as well as in the High Performance Computing Center of the Universidad Nacional de Córdoba (CCAD-UNC). This research was funded by CONICET and Secyt/UNC.

References

Andoyer, H. 1903, Bull. Astron. Ser. I, 20, 321
Baruteau, C., Crida, A., Paardekooper, S.-J., et al. 2014, in Protostars and Planets VI, eds. H. Beuther, R. S. Klessen, C. P. Dullemond, & T. Henning (Tucson: University of Arizona Press), 667
Beaugé, C. 1994, Celest. Mech. Dyn. Astron., 60, 225
Beaugé, C., & Michtchenko, T. A. 2003, MNRAS, 341, 760
Beaugé, C., Michtchenko, T. A., & Ferraz-Mello, S. 2006, MNRAS, 365, 1160
Beaugé, C., Gianuzzi, E., Trógolo, N., et al. 2025, A&A, 702, L15
Beutler, G. 2005, Methods of Celestial Mechanics (Berlin: Springer)
Braga-Ribas, F., Sicardy, B., Ortiz, J. L., et al. 2013, ApJ, 773, 26
Dvorak, R., Pilat-Lohinger, E., Schwarz, R., & Freistetter, F. 2004, A&A, 426, L37
Fraser, W. C., Batygin, K., Brown, M. E., & Bouchez, A. 2013, Icarus, 222, 357
Henrard, J., & Lemaitre, A. 1983, Celest. Mech., 30, 197
Kiss, C., Müller, T. G., Marton, G., et al. 2024, A&A, 684, A50
Lee, M. H., & Peale, S. J. 2002, ApJ, 567, 596
Lee, M. H., & Peale, S. J. 2003, ApJ, 592, 1201
Message, P. J. 1958, AJ, 63, 443
Morbidelli, A., & Moons, M. 1993, Icarus, 102, 316
Morgado, B. E., Sicardy, B., Braga-Ribas, F., et al. 2021, A&A, 652, A141
Morgado, B. E., Sicardy, B., Braga-Ribas, F., et al. 2023, Nature, 614, 239
Moriwaki, K., & Nakagawa, Y. 2004, ApJ, 609, 1065
Ortiz, J. L., Gutiérrez, P. J., Sota, A., Casanova, V., & Teixeira, V. R. 2003, A&A, 409, L13
Ortiz, J. L., Santos-Sanz, P., Sicardy, B., et al. 2017, Nature, 550, 219
Pereira, C. L., Sicardy, B., Morgado, B. E., et al. 2023, A&A, 673, L4
Pereira, C. L., Braga-Ribas, F., Sicardy, B., et al. 2025, ApJ, 992, L19
Ramos, X. S., Charalambous, C., Benítez-Llambay, P., & Beaugé, C. 2017, A&A, 602, A101
Regály, Z., Fröhlich, V., & Kiss, C. 2025, PASP, 137, 114401
Salo, H., Sicardy, B., Mondino-Llermanos, A., et al. 2021, European Planetary Science Congress, EPSC2021, 338
Sicardy, B., Leiva, R., Renner, S., et al. 2019, Nat. Astron., 3, 146
Sicardy, B., Salo, H., El Moutamid, M., Renner, S., & Souami, D. 2025, A&A, 704, A23